materials proceedings

MDPI

Proceeding Paper

Microstructural and Phase Integrity of 3D-Printed High-Purity Alumina for Bio-Inspired Dental Implants †

Emmanuel Munenge [1,*], Winnie Mtetwa [1], Harry Ngwangwa [1], Thanyani Pandelani [1] and Lebogang Lebea [2]

[1] Department of Mechanical, Bioresources and Biomedical Engineering, College of Science, Engineering and Technology, University of South Africa, Florida 1710, South Africa; 54903076@mylife.unisa.ac.za (W.M.); ngwanhm@unisa.ac.za (H.N.); epandet@unisa.ac.za (T.P.)

[2] Department of Mechanical and Mechatronics Engineering, Faculty of Engineering and Built Environment, and Information Technology, Central University of Technology, Bloemfontein 9300, South Africa; llebea@cut.ac.za

* Correspondence: 44518870@mylife.unisa.ac.za

† Presented at the 4th International Conference on Applied Research and Engineering, Pretoria, South Africa, 21–23 November 2025.

Abstract

High-purity α-Al_2O_3 ceramics are widely used in dental applications due to their excellent mechanical strength and biocompatibility; however, maintaining phase stability and microstructural integrity during 3D printing remains challenging. In this study, bio-inspired dental implants were fabricated using lithography-based ceramic manufacturing (LCM) and characterized structurally and mechanically. XRD confirmed phase-pure α-Al_2O_3 with high crystallinity, an average crystallite size of 28.68 nm, and low compressive microstrain. SEM revealed uniform, fine equiaxed grains (4.60 ± 0.28 µm) with good densification. The implants exhibited a Vickers hardness of 15.49 GPa and compressive strength of 991.5 MPa, demonstrating suitability for load-bearing dental applications. These findings demonstrate that lithography-based ceramic manufacturing (LCM) produces phase-pure and microstructurally uniform implants, confirming its viability for manufacturing bio-inspired dental implants with reliable mechanical performance.

Keywords: alumina (Al_2O_3); dental implants; crystallite size; x-ray diffraction (XRD); lattice strain

1. Introduction

Alumina (Al_2O_3) is a longstanding material in biomedical ceramics owing to its high chemical stability, wear resistance, and mechanical strength. Its high purity further enhances its suitability for dental implant applications [1,2]. Traditional processing techniques such as Computer-Aided Design/Computer-Aided Manufacturing (CAD/CAM) milling, while established, often fall short when intricate, bio-inspired geometries are required [3]. Additive manufacturing (AM), particularly lithographic ceramic manufacturing (LCM), offers a compelling alternative for fabricating complex ceramic structures [4]. LCM is a photopolymerization-based technique derived from digital light processing (DLP), known for its high precision and reproducibility [5].

Bio-inspired design strategies such as those mimicking trabecular bone structures or the tapered morphology of natural tooth roots are increasingly explored to improve osseointegration and load transfer at the bone–implant interface. These approaches leverage natural biological architectures to improve the interaction between implants and surrounding bone tissue, leading to better mechanical stability and integration [6]. AM technologies like

Check for updates

Academic Editor: Tiyamike Ngonda

Published: 13 April 2026

Copyright: © 2026 by the authors. Licensee MDPI, Basel, Switzerland. This article is an open access article distributed under the terms and conditions of the Creative Commons Attribution (CC BY) license.

LCM make it feasible to replicate such features in ceramic components while maintaining dimensional accuracy, reduced material waste and design freedom [4]. While hierarchical microstructuring of dense ceramics has recently gained attention for enhancing mechanical performance [7], its implementation in alumina systems is still evolving. In particular, the use of functionally oriented porosity, such as obliquely angled blind pores intended for biological interfacing, remains comparatively underexplored in dense or partially porous alumina materials. The bio-inspired pore orientation and geometry in this study were designed based on trabecular bone anisotropy, where pore orientation aligns with principal stress directions to balance mechanical strength and biological functionality [8]. The oblique orientation promotes mechanical interlocking and stress redistribution, while blind pores at the surface enable cell ingress and vascularization without compromising the dense core's load-bearing capacity. This reflects the trade-off between biological access and mechanical integrity observed in scaffold design, where pore size and distribution substantially influence both cellular behavior and structural performance [9].

Lithalox 350D alumina was selected as the base material. This grade is a high-purity, fine-grained α-Al_2O_3 engineered specifically for technical ceramics with excellent mechanical and dielectric properties. Lithalox 350D is known for its high sinterability and dimensional stability, making it particularly well-suited for precision parts such as dental implants [10]. Its purity level (>99.8%) minimizes the risk of secondary phase formation during sintering and enhances long-term biocompatibility [11]. These attributes align with results from Schwentenwein & Homa [12], who demonstrated that lithography-based additive manufacturing of alumina ceramics via LCM can produce parts with over 99% theoretical density and high mechanical integrity under precision conditions. However, limited data are available regarding its behavior during LCM processing, especially concerning phase retention and microstructural evolution after sintering.

Ensuring phase stability during fabrication is critical for the mechanical reliability of ceramic implants [13]. The presence of defects introduced during various fabrication processes can significantly affect the performance of ceramic materials. For example, Li et al. [14] demonstrated that variations in the debinding atmosphere during stereolithography-based three-dimensional printing of Al_2O_3 ceramics can lead to the formation of defects such as nonuniform porosity and internal stresses that directly impair mechanical integrity. Optimizing these processes and understanding the sources of defects are essential for enhancing the mechanical properties and longevity of ceramic implants.

The alumina microstructure can undergo notable transformations due to localized thermal gradients during sintering, influencing grain growth, porosity, and mechanical performance. For instance, Kermani et al. [15] reported that rapid heating rates can significantly retard grain growth in MgO-doped alumina by altering thermal histories and diffusion kinetics. To assess phase composition and processing-induced effects, X-ray diffraction (XRD) serves as a non-destructive technique to confirm the presence of α-phase alumina and to detect phase impurities or residual stresses [16]. This method delivers detailed insights into crystalline structure and stress distribution, which are crucial for predicting material performance and failure modes [17]. Additionally, microstructural analysis through optical imaging allows for evaluation of grain size distribution, surface integrity, and potential defects that may impact implant longevity. This analysis can reveal critical insights into the material properties and performance of implants, which directly influence their durability and functionality [18].

Material durability is further governed by microstructural stability under environmental exposure. Srinivasan et al. [19] showed that hygrothermal aging can significantly alter mechanical behavior due to microstructural degradation, emphasizing the importance of structure–property relationships relevant to dental implant service conditions. Alongside

durability considerations, sustainability and advanced manufacturing are increasingly central to material research. Bernard et al. [20] demonstrated that bio-based constituents can be incorporated into engineering materials without compromising performance, while Faisal et al. [21] highlighted sustainability, digitalization, and customization within Industry 5.0-based manufacturing frameworks applicable to ceramic additive manufacturing. Additive manufacturing enables material-efficient fabrication and design flexibility across high-performance sectors [22], and growing interest in sustainable and bio-inspired material systems further supports nature-inspired design approaches [23]. In this context, lithography-based ceramic manufacturing offers sustainability advantages over subtractive ceramic processing through near-net-shape fabrication, reduced material waste, and minimized post-processing.

While the recent literature indicates a growing interest in lithography-based ceramic manufacturing for dental applications, there are critical knowledge gaps yet to be addressed. For instance, most studies tend to focus on conventional implant design geometries without biological design consideration. The present study addresses this gap by focusing on a bio-inspired novel Lithalox 350D alumina pore architecture featuring obliquely angled blind pores oriented at approximately 45° to the implant axis. The orientation mimics the anisotropic trabecular bone structure and aligns with principal stress directions during mastication. Furthermore, this study provides the first comprehensive phase stability validation using comprehensive material science characterization techniques including X-ray diffraction (XRD), scanning electron microscopy (SEM), compression testing and Vickers hardness testing. The findings aim to support the development of robust, bio-inspired alumina ceramic implants tailored for advanced dental applications through additive manufacturing.

2. Materials and Methods

2.1. Materials and 3D Printing

The material used in this study was Lithalox 350D alumina, a high-purity α-Al_2O_3 ceramic. Bio-inspired dental implant test specimens, with a cylindrical geometry measuring 22 mm in length and 4 mm in diameter, were fabricated via 3D printing by CADdent® GmbH (Augsburg, Germany) using a CeraFab S65 printer by Lithoz GmbH in Vienna, Austria. The printer operates based on lithography-based ceramic manufacturing (LCM) technology, providing a lateral (XY) resolution of 40 µm and a layer thickness of 25 µm. The alumina ceramic slurry was photopolymerized layer-by-layer using UV light (λ = 460 nm), selectively curing the material at designated locations to encapsulate the ceramic particles within the printed structure. Printing parameters were optimized for consistency and quality, with a digital light processing (DLP) energy of 170 MJ/cm^2 per layer. A bio-inspired pore architecture was incorporated into the specimen design, consisting of multiple blind-hole pores oriented obliquely relative to the implant axis and confined to a localized porous zone near the apical end. All specimens for this study were fabricated in a single print batch to maintain consistency in processing parameters. The specimens obtained were then subjected to post-processing and characterized using different techniques such as X-ray diffraction and SEM. The experimental methodology is summarized in Figure 1.

https://doi.org/10.3390/materproc2026031014

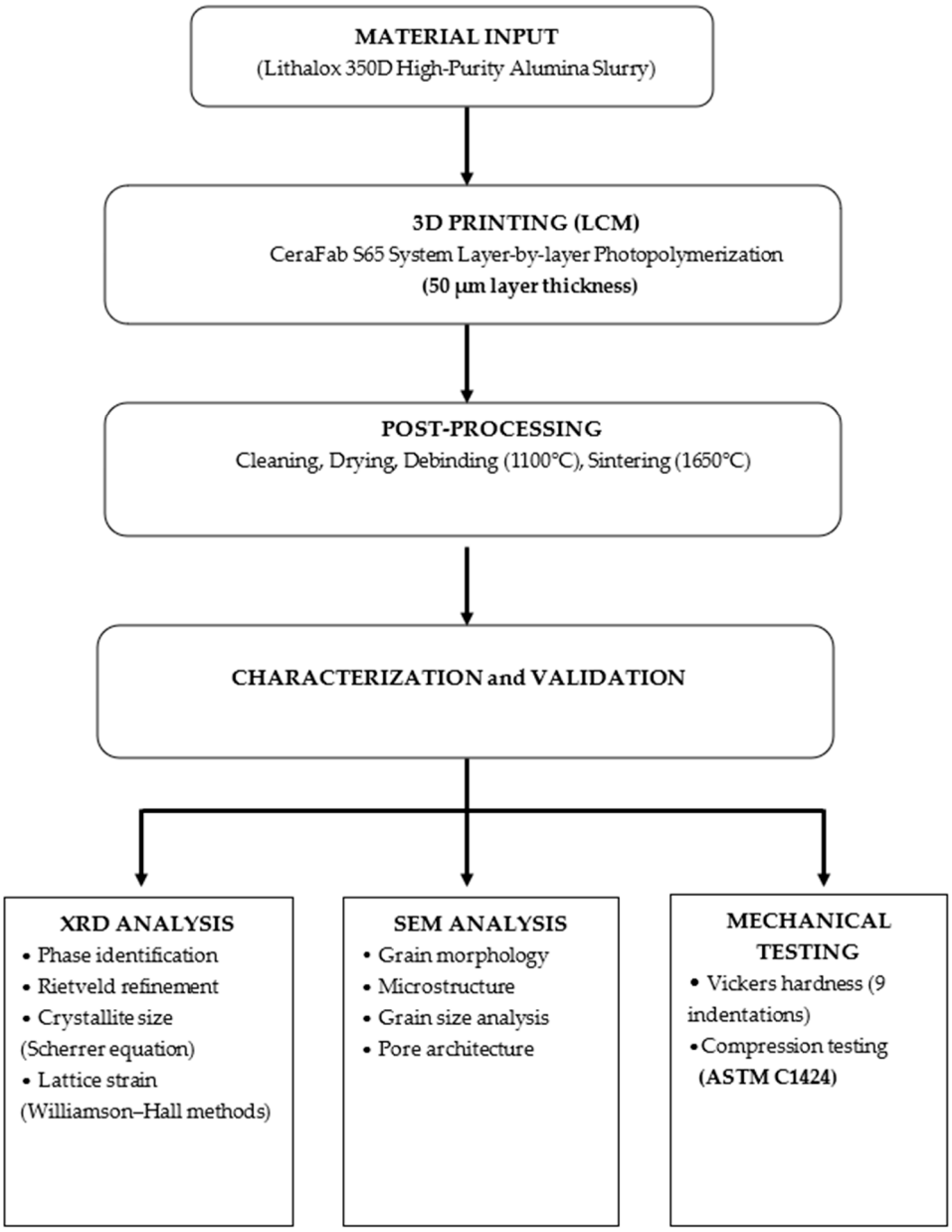


Figure 1. Experimental methodology flowchart.

2.2. Post-Processing and Sintering

After printing, the green parts underwent thermal debinding at 1100 °C to remove organic binders, followed by sintering in a laboratory high-temperature chamber furnace (LHTCF) at 1650 °C. These conditions were selected to ensure complete densification, maintain α-phase stability, and minimize grain coarsening of the final ceramic test specimens.

2.3. X-Ray Diffraction (XRD) Analysis

X-ray diffraction (XRD) analysis was performed using a Rigaku SmartLab high-resolution diffractometer (Rigaku Corporation, Tokyo, Japan), (Figure 2) equipped with a sealed Cu Kα radiation source (λ = 1.541874 Å). The X-ray tube operated at 20–40 kV and 2–44 mA, with a nominal power output of approximately 3 kW, producing monochromatic X-rays via electron bombardment of a copper target. The generated beam was directed toward the sample, and diffracted intensities were recorded by a scintillation detector mounted on a goniometer, which precisely controlled the angular positions of both the sample and detector. Scans were carried out over a 2θ range of 10–90°, with a step size

of 0.02° and a scan rate of 1°/min. To reduce preferred orientation effects and improve statistical reliability, the sample stage was continuously rotated at approximately 1 revolution per second during acquisition. Peak positions, intensities, and full width at half maximum (FWHM) values were extracted from selected Bragg reflections. Data were processed using PDXL version 2.0 software (Rigaku Corporation, Tokyo, Japan). Phase identification was conducted by comparing experimental patterns with entries from the PDF-4+ database (ICDD, Newtown Square, PA, USA), with reference to ICDD card No. 96-900-8082 for α-Al_2O_3 (trigonal symmetry, space group R-3c, No. 167). Quantitative phase refinement was further done using Diamond version 5.1.0 software (Crystal Impact GbR, Bonn, Germany) and a refined lattice model of α-Al_2O_3 was generated.

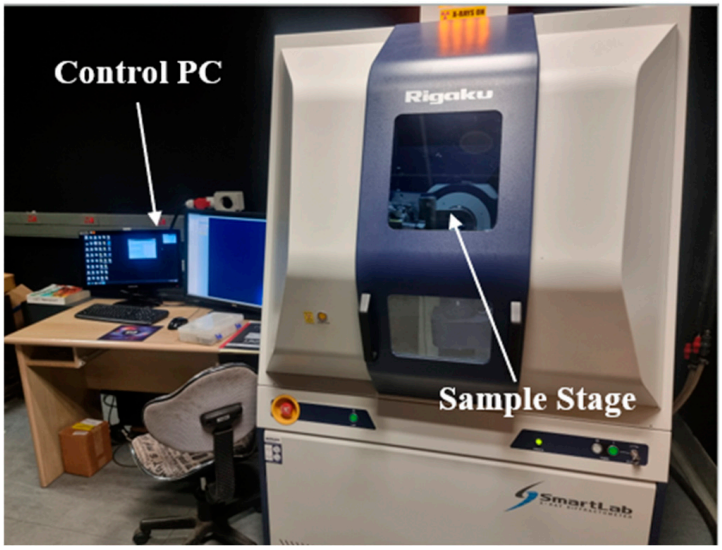


Figure 2. Rigaku SmartLab high-resolution X-ray diffractometer used for XRD analysis.

The average crystallite size (D) and lattice microstrain (ε) were calculated using the Williamson–Hall (W-H) plot method. The W–H approach is based on the following equation [24]:

$$\beta\cos\theta = \left(\frac{k\lambda}{D}\right) + 4\varepsilon\sin\theta \quad (1)$$

where β is the full width at half maximum (FWHM) in radians, θ is the Bragg angle, λ is the X-ray wavelength, D is the crystallite size, and ε is the microstrain. The microstrain is the gradient and D is calculated from the y-intercept of the W-H plot of $\beta\cos\theta$ vs. $4\sin\theta$.

2.4. Microstructure Characterization

Alumina ceramic samples were mounted using a Struers CitoPress-15 hot mounting machine and subsequently polished using a Struers automatic polishing machine (Struers, Champigny Sur-Marne, France) following a standard three-step metallographic procedure. Planar grinding was performed on a Struers Piano 220 surface with water for 4 min 30 s, followed by fine polishing on a Plan cloth using a DiaPro Plan 9 µm diamond suspension for 15 min. Final polishing was completed on a Chem cloth with an OP-S colloidal silica suspension (0.04 µm) for 45 s to achieve a deformation-free, mirror-like finish. After polishing, the samples were rinsed with distilled water, cleaned with ethanol, and subsequently air-dried under ambient conditions. Microstructural analysis was performed using a Zeiss Gemini 340 Crossbeam scanning electron microscope (SEM) (Carl Zeiss GmbH, Oberkochen, Germany). High-resolution images were obtained at various magnifications, and surface morphology was quantitatively analyzed using Zeiss Smart SEM Version 6.03 software. The SEM was operated at an EHT (Electron High Tension) of 3.00 kV with a

working distance (WD) of 20.5 mm. The SEM images were further analyzed using ImageJ version 1.54m software to determine the average grain sizes. Measurements were done on 110 equiaxed grains.

2.5. Vickers Hardness Testing

Hardness measurements were conducted on three specimens in accordance with ISO 14705:2016, [25]. A Zwick Roell Indentec ZHV hardness tester (Zwick GmbH, Ulm, Germany), equipped with a diamond pyramid indenter (apex angle of 136°), was used to perform the indentations. Considering the size and geometry of the dental implant samples, a load of 9.81 N (1 kgf) was applied with a dwell time of 10 s. The mean Vickers hardness (VHV) for each specimen was calculated from the three measurements, and the standard deviation was determined to quantify measurement variability. The diagonal lengths of the indentations were measured using an optical microscope coupled with a Zeiss Smart Zoom 5 image analysis system. The Vickers hardness number (VHV) was obtained using Equation (2).

$$\mathrm{VHV} = 1.854\frac{\mathrm{P}}{\mathrm{d}^2} \quad (2)$$

where P is the applied load (N) and d is the length of the diagonals in mm [26].

The VHV values were subsequently converted into SI units (GPa) using a multiplication factor of 0.009807, as recommended in [27], to ensure consistency across the literature.

2.6. Compression Testing

Compression tests were conducted using an Instron 8801 servo-hydraulic testing machine, with a 100 kN load capacity and an operational accuracy of ±0.5%. The system was controlled via a digital 8800 MT controller, providing complete control throughout the experimental process. A displacement control mode was used to apply compressive load with a constant crosshead loading rate of 0.5 mm/min until fracture occurred. Compression tests were carried out in accordance with ASTM C1424-15R19 (Standard Test Method for Monotonic Compressive Strength of Advanced Ceramics at Ambient Temperature) [28]. A total of five specimens were tested for statistical reliability.

3. Results and Discussion

3.1. X-Ray Diffraction Analysis

The XRD pattern of the test sample, as shown in Figure 3, exhibited sharp and well-defined peaks. Prominent diffraction peaks were observed at 2θ values of 25.55°, 35.15°, 37.80°, 43.35°, 52.55°, 57.50°, 66.50°, 68.20°, and 76.90°, corresponding to the Miller indices (102), (104), (110), (113), (204), (116), (214), (300), and (119), respectively, as summarized in Table 1. These peaks are characteristic of the α-Al_2O_3 (alpha-alumina) phase, as per comparison to the PDF-4+ database ICDD card #96-900-8082. The α-Al_2O_3 phase is the most thermodynamically stable and mechanically robust polymorph of alumina. The most intense peak was observed at 2θ = 57.50°, corresponding to the (116) crystallographic plane, with an intensity value of 18,662.18 a.u. This pronounced peak suggests a preferred orientation along this plane and indicates a high degree of crystallinity [29,30].

The presence of sharp, well-defined diffraction peaks is characteristic of well-crystallized corundum. This observation aligns with previous findings that associate strong Bragg reflections with the formation of corundum structures [31]. The mechanical and chemical stability associated with α-Al_2O_3 has been widely documented. This is consistent with the intense Bragg reflections reported for well-crystallized corundum [32]. The α-phase, known for its thermal stability, hardness, and chemical resistance, has also been confirmed [33]. Moreover, phase stability in ceramic materials has been shown to

significantly enhance fracture resistance [34]. These findings support the potential of the synthesized α-alumina for load-bearing dental applications, where high crystallinity is crucial for long-term performance [35].

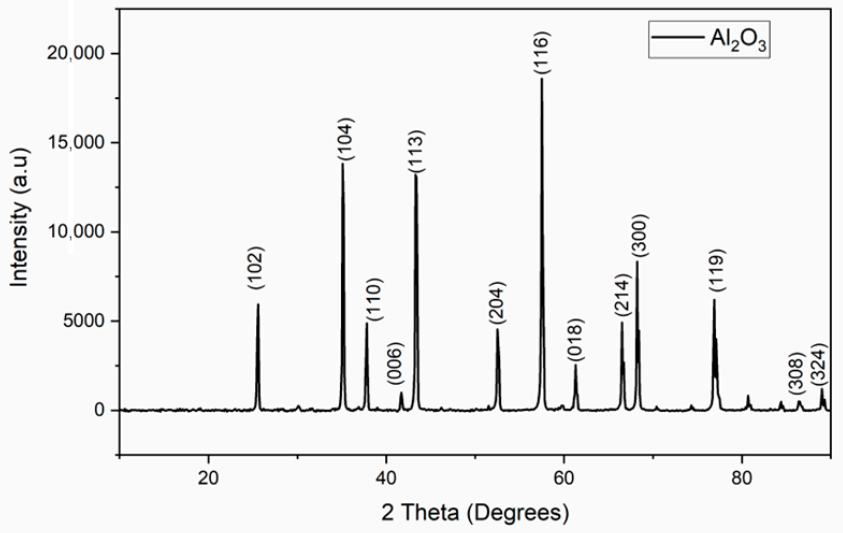


Figure 3. X-ray diffractogram pattern of Al_2O_3 showing characteristic peaks of the corundum phase (α-Al_2O_3).

Table 1. X-ray diffraction pattern of synthesized α-alumina.

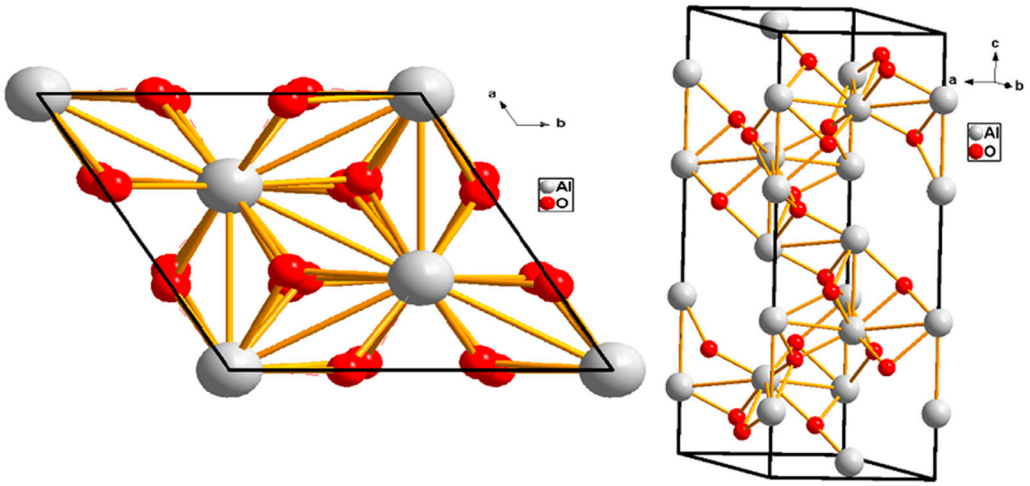
2θ (°)	d (Å)	Relative Intensity I/I0	Counts (cps)	FWHM (°)	Plane (hkl)
25.55	3.4836	346.3	1761	0.7826	102
35.15	2.5510	848.8	4316	0.3740	104
37.80	2.3781	259.3	1319	0.3236	110
43.35	2.0856	892.4	4538	0.4185	113
52.55	1.7401	260.1	1323	0.3413	204
57.50	1.6015	1000.0	5086	0.6637	116
66.50	1.4049	229.8	1169	0.2637	214
68.20	1.3740	384.1	1953	0.5300	300
76.90	1.2388	318.2	1618	0.4969	119

The effectiveness of the lithography-based ceramic manufacturing (LCM) process, combined with sintering at 1650 °C, in preserving the α-phase was evident. It has been reported that increasing the sintering temperature of zirconia-toughened alumina (ZTA) from 1450 °C to 1650 °C improves density, mechanical strength, hardness, and wear performance [2]. Furthermore, LCM has been shown to produce dense, defect-free ceramics with tailored microstructures suitable for implants [36]. The near-complete retention of the α-phase demonstrates the reproducibility and reliability of LCM for high-purity biomedical ceramic dental implants.

3.2. Unit Cell Volume and Crystal Structure Analysis

The unit cell volume was calculated to be 254.79 $Å^3$ using Diamond software (Crystal Impact GbR, Bonn, Germany). This value is in excellent agreement with the theoretical volume of 255.37 $Å^3$ reported for pure hexagonal α-alumina [37]. The negligible deviation between the calculated and theoretical values confirms the preservation of the characteristic corundum structure, indicating that the additive manufacturing process and subsequent sintering did not alter the crystallographic integrity or phase purity of α-Al_2O_3. Further-

more, to provide a fundamental understanding of the α-Al_2O_3 crystal structure, Diamond software was used to generate structural models of α-Al_2O_3 based on the corundum crystal structure with rhombohedral symmetry (space group R$\overline{3}$c, No. 167), as shown in Figure 4a,b. Figure 4a illustrates the primitive unit cell, in which aluminum atoms are octahedrally coordinated by oxygen atoms to form distorted AlO_6 units arranged in a three-dimensional hexagonal close-packed lattice. This atomic arrangement represents the fundamental structural framework of α-alumina.



(**a**) (**b**)

Figure 4. (**a**) Primitive unit cell of α-Al_2O_3, illustrating the core AlO_6 octahedral coordination that forms the fundamental building blocks of the corundum structure. (**b**) Extended supercell of α-Al_2O_3 based on the R$\overline{3}$c (#167) space group, showing the periodic stacking of multiple unit cells in a dense, hexagonal, close-packed lattice.

Figure 4b shows an extended supercell constructed by stacking multiple unit cells along the c-axis, highlighting the long-range periodicity and dense packing characteristic of the corundum structure. The lattice parameters determined in this study were a = 4.75890 Å and c = 12.99100 Å, yielding a c/a ratio of 2.73. These values are in excellent agreement with reported data for α-alumina [34], confirming the accuracy of the crystallographic model and the preservation of the thermodynamically stable α-phase. The absence of significant deviation in unit cell volume further indicates that no transformation to metastable alumina polymorphs, such as γ- or θ-Al_2O_3, occurred during processing [38].

3.3. Crystallite Size and Microstrain (Williamson–Hall) Analysis

A linear relationship was observed between βcosθ and 4sinθ, as shown in Figure 5, confirming that both crystallite size and microstrain contributed to the broadening of XRD peaks in the synthesized α Al_2O_3 ceramic.

The plot exhibited strong linearity, with a coefficient of determination (R^2) of 0.95278, indicating a good fit to the Williamson–Hall model. The y-intercept of the plot yielded an average crystallite size of 28.68 nm, while the slope indicated a microstrain (ε) of −0.00137 (-1.37×10^{-3}), as summarized in Table 2. These values reflect a highly crystalline structure with minimal lattice distortion, an important attribute for ensuring mechanical stability in dental applications. The measured crystallite size falls within the optimal range for dental ceramics (20 to 100 nm), which has been shown to enhance both fracture toughness and wear resistance. These are critical properties that influence the durability and performance of implants under cyclic mastication and exposure to the oral environment [39,40].

Table 2. Summary of Williamson–Hall analysis parameters.

Parameter	Value
Intercept	0.0051 ± 0.0002
Slope	−0.0014 ± 0.0001
Pearson's r	−0.97912
R-Square (COD)	0.95868
Adj. R^2	0.95278

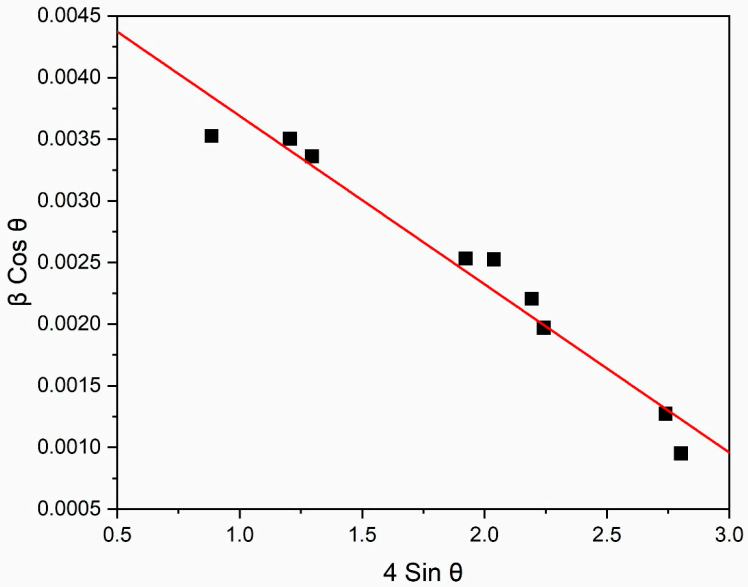


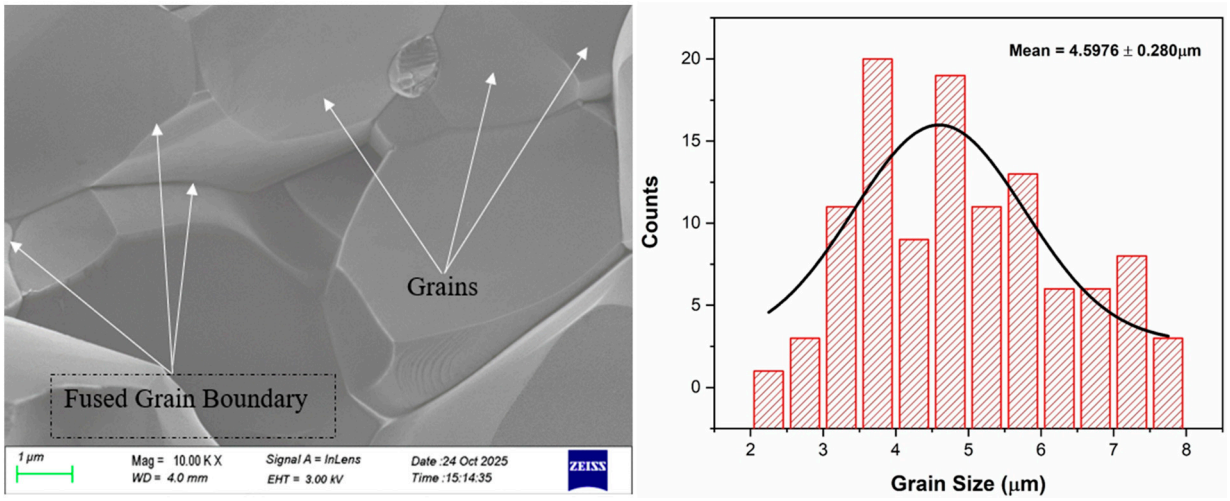
Figure 5. Williamson–Hall plot (βcosθ vs. 4sinθ) for the synthesized α-Al_2O_3 ceramic.

The Williamson–Hall analysis revealed a low microstrain, indicating minimal lattice distortion and low residual internal stresses, as inferred from XRD peak broadening. In XRD theory, lower microstrain corresponds to reduced crystallographic lattice perturbations, which are often linked to fewer internal defects and a more stable microstructure. Reduced internal stress states have been shown to mitigate fatigue crack initiation and slow crack propagation under cyclic loading, thereby enhancing fatigue resistance in load-bearing materials [41,42]. Dimensional stability and fatigue resistance, which are influenced by microstrain, are especially important for dental implants subjected to repetitive loading in moist oral conditions. Similar studies in alumina-based nanocomposites reported very low lattice distortion (<0.2% microstrain) in alumina templates, indicating that minimized internal stress is beneficial for structural performance [43]. Additionally, a small degree of microstrain may increase surface reactivity, enhancing protein adsorption and cell attachment, both of which support effective osseointegration. Overall, the low microstrain observed in this study suggests favorable mechanical reliability and biological performance for dental implant applications.

3.4. Surface Characterization

Figure 6a shows a high-magnification SEM image (10.00 kX) of the sintered alumina specimens, revealing a compact, well-densified surface with uniformly distributed grains and clearly fused grain boundaries. The dense and homogeneous microstructure, with minimal intergranular cracking or surface defects, indicates that sintering at 1650 °C achieved efficient densification. No visible layer lines, microcracks, or staircase effects commonly associated with additive manufacturing were detected, demonstrating the excellent surface resolution and geometric precision of the LCM process. Such microstructural uniformity is

critical for ensuring high compressive strength, fracture toughness, and wear resistance, key attributes for dental implant applications [44,45].



(**a**) (**b**)

Figure 6. (**a**) SEM micrograph of sintered 3D-printed alumina ceramics at high magnification (10.00 kX) showing well-fused grain boundaries and dense microstructure; (**b**) grain size distribution of sintered 3D-printed alumina specimens obtained from ImageJ analysis (n = 110 grains).

A few pores and voids were present which were likely formed from residual gas entrapment or incomplete densification during the final sintering stage. Voids and pores can serve as local stress concentration sites or initiation points for fatigue under mechanical loading, potentially promoting crack initiation and propagation [46,47]. The voids and pores noted in this study were minimal, indicating limited influence on the mechanical strength of the implant.

Further analysis of the SEM images at 5.00 kX magnification using ImageJ software was conducted to determine the average grain size. Measurements on 110 equiaxed grains revealed sizes ranging from 2 to 8 µm, with a mean of 4.598 ± 0.280 µm (Figure 6b). The narrow grain size distribution indicates uniform grain growth during sintering, facilitated by a total heating duration of 9.5 h with a 2 h dwell time. These parameters promoted effective densification while preventing exaggerated grain coarsening. The measured grain size closely aligns with values reported for conventionally sintered high-purity alumina ceramics, such as 5.63 µm at 1600 °C [48]. These results demonstrate that LCM can produce bio-inspired microstructures with uniform grain sizes comparable to traditional methods, highlighting its potential for manufacturing high-quality alumina ceramics for biomedical applications.

3.5. Vickers Hardness

The measured Vickers hardness values of the 3D-printed alumina specimens ranged from 15.44 to 15.50 GPa, with an average of 15.48 ± 0.020 GPa (1578.02 HV) (Figure 7). The low standard deviation of 0.034 indicates minimal variation among samples, reflecting the high consistency and repeatability of the additive manufacturing process. The narrow range also suggests a high degree of densification and a uniform microstructure, with negligible influence from inherent porosity or layering effects.

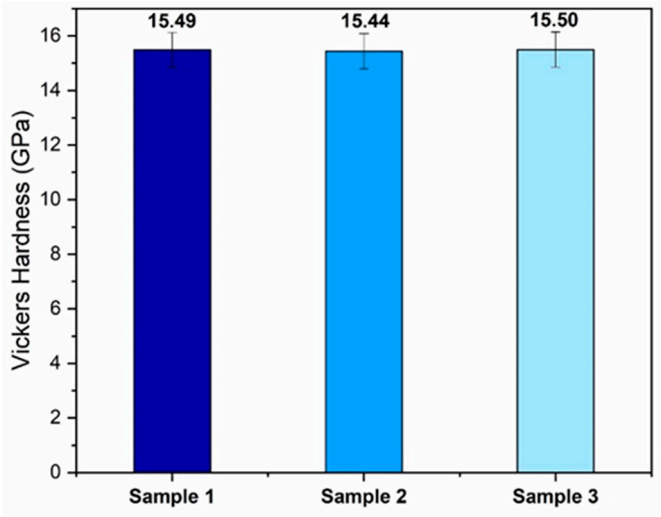


Figure 7. Average Vickers hardness values of the test samples. Error bars represent the standard deviation from multiple indentations per specimen.

These hardness values fall within the expected range for dense sintered alumina ceramics [49] and exceed typical values reported for dental zirconia, which generally range from 1200 to 1500 HV depending on yttria content and processing conditions [50,51]. The elevated and uniform hardness indicates superior wear resistance and mechanical durability, essential for components subjected to repetitive masticatory forces. Notably, conventional alumina dental implants typically exhibit Vickers hardness values of 1800–2000 HV, indicating that the present LCM-fabricated alumina samples achieved comparable mechanical performance despite the presence of bio-inspired central pores [51,52]. Notably, the presence of bio-inspired central pores did not cause a significant reduction in hardness, consistent with observations in LCM-fabricated dental zirconia components [52]. These results indicate that the LCM process preserves sufficient mechanical integrity for dental applications while enabling bio-inspired porosity, supporting structural stability and potential long-term clinical performance.

3.6. Compression Testing

The compression data obtained from the stress–strain graph (Figure 8) analysis offer valuable insights into the mechanical behavior of the alumina (Al_2O_3) specimens under uniaxial loading. The stress–strain response exhibits a sharp, linear increase followed by a sudden drop in stress, indicative of brittle fracture after elastic deformation. This behavior is attributable to the atomic bonding structure of ceramics, which lack mobile dislocations and do not exhibit plastic deformation prior to failure. In clinical oral environments, implants are mainly exposed to compressive and cyclic masticatory loads rather than monotonic uniaxial loading. Although the brittle nature of alumina limits its tolerance to tensile stresses, its high compressive strength is compatible with physiological biting forces when appropriate implant design and load distribution are achieved.

The compressive stress–strain curve confirms the high compressive strength of the alumina specimens, with peak stresses reaching a maximum of 1244.54 MPa. This high strength value makes the material well-suited for biomedical applications, particularly dental implants, which typically experience compressive loads of approximately 100–300 MPa during mastication [53]. Alumina ceramics used in implantology typically exhibit compressive strengths ranging from 572 to 2500 MPa, depending on microstructure and processing methods [2,49]. The mean compressive strength of 991.51 MPa observed in this study falls comfortably within this range, indicating that the 3D printing and post-processing protocols employed yielded mechanically robust implants. These elevated values under-

score alumina's suitability for dental applications, where materials must endure substantial masticatory forces typically encountered in the oral cavity. Piconi and Sprio [54] similarly reported that high-purity, fine-grained, third-generation alumina exhibits a flexural strength of approximately 630 MPa, supporting the present findings. Overall, the compression test data indicates the feasibility of alumina as an alternative material for dental implants.

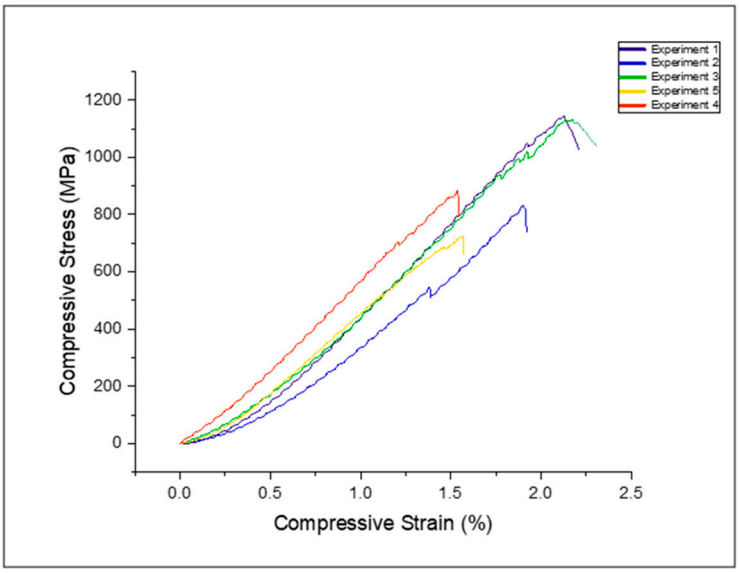


Figure 8. Compressive stress–strain graph of 3D-printed alumina (Al_2O_3) specimens showing the mechanical response under uniaxial loading.

4. Conclusions

High-purity, bio-inspired α-Al_2O_3 dental implants were successfully fabricated using lithography-based ceramic manufacturing (LCM) and sintering at 1650 °C. XRD confirmed phase-pure α-Al_2O_3 with high crystallinity, an average crystallite size of 28.68 nm, low compressive microstrain of 1.37×10^{-3}, and a unit cell volume of 254.79 $Å^3$. SEM revealed uniform, fine equiaxed grains (4.60 ± 0.28 μm) with good densification and defect-free surfaces. The implants exhibited a Vickers hardness of 15.49 GPa and compressive strength of 991.5 MPa, confirming their suitability for load-bearing dental applications. These findings demonstrate LCM as a reliable technique for producing structurally stable, high-performance α-Al_2O_3 ceramics for dental and orthopedic implants. This study further proves that LCM is a viable alternative to conventional ceramic processing methods, offering the advantages of structural integrity and unique implant design aligned with the human dental structure.

5. Future Work

Building on the present analysis of crystallite size, lattice strain, dislocation unit cell volume, surface microstructure, compression tests and Vickers hardness, future studies should focus on several key areas. Firstly, computational fatigue simulations should be conducted using user-defined material subroutines (e.g., VUMAT) in finite element analysis incorporating dislocation density and lattice strain data to predict implant lifespan under cyclic loading. Secondly, quantitative measurement of surface roughness parameters such as Ra and Rz are needed to evaluate the influence of surface roughness parameters on biological response and mechanical fatigue resistance. Thirdly, ex vivo fatigue and wear experiments simulating oral conditions should be conducted to validate computational predictions and evaluate implant durability. Moreover, in vitro cell viability and proliferation

studies can help to assess the biocompatibility and suitability of the material for real-life applications.

These future directions will help advance the development of robust, biocompatible alumina dental implants with improved long-term clinical performance.

6. Patents

The 3D-printed dental implant test specimen is under patent application number 2024/06400 filed with the Companies and Intellectual Property Commission of South Africa.

Author Contributions: E.M. and W.M. conducted the experimental work, including Vickers hardness testing, compression testing, X-ray diffraction (XRD), and microstructural analysis. The data analysis and manuscript writing were also greatly aided by their contributions. H.N., L.L. and T.P. oversaw the study, gave technical advice, and edited the report. All authors have read and agreed to the published version of the manuscript.

Funding: This research was funded and supported by the Directorate of Innovation, Technology Transfer and Commercialization under the Technology Innovation Agency grant at the University of South Africa.

Institutional Review Board Statement: Not applicable.

Informed Consent Statement: Not applicable.

Data Availability Statement: The literature contains all of the data used in this work, and the appropriate references have been supplied accordingly.

Acknowledgments: The authors would like to thank the University of South Africa's Directorate of Innovation, Technology Transfer and Commercialization for their financial support from Technology Innovation Agency.

Conflicts of Interest: The authors declare no conflict of interest.

Abbreviations

The following abbreviations are used in this manuscript:

3D	Three-Dimensional
AM	Additive Manufacturing
CPS	Counts per Second
CAD/CAM	Computer-Aided Design/Computer-Aided Manufacturing
DLP	Digital Light Processing
ICDD	International Centre for Diffraction Data
ISO	International Organization for Standardization
LCM	Lithographic Ceramic Manufacturing
LHTCF	Laboratory High-Temperature Chamber Furnace
SEM	Scanning Electron Microscopy
VHN	Vickers Hardness Number
XRD	X-ray Diffraction

References

1. Kavya, K.; Sharanraj, V.; Ramesh, C.M.; Kumar M, N.; Kumar, V.; Mariyaiah, S.; Kumar, T.A.; Chandan, B.R. Alumina: As a Biocompatible Biomaterial Used in Dental Implants. *J. Dent. Appl.* **2022**, *8*, 472–476. [CrossRef]
2. Zhu, L.; Xu, Y.; Liu, S.; Chen, H.; Tao, J.; Tong, X.; Li, Y.; Huang, S.; Lin, J.; Wen, C.; et al. Microstructure, mechanical properties, friction and wear performance, and cytotoxicity of additively manufactured zirconia-toughened alumina for dental applications. *Compos. Part B Eng.* **2023**, *250*, 110459. [CrossRef]
3. Raheem, A.A.; Hameed, P.; Whenish, R.; Elsen, R.S.; G, A.; Jaiswal, A.K.; Prashanth, K.G.; Manivasagam, G. A review on development of bio-inspired implants using 3d printing. *Biomimetics* **2021**, *6*, 65. [CrossRef] [PubMed]

4. Scheithauer, U.; Schwarzer, E.; Moritz, T.; Michaelis, A. Additive Manufacturing of Ceramic Heat Exchanger: Opportunities and Limits of the Lithography-Based Ceramic Manufacturing (LCM). *J. Mater. Eng. Perform.* **2018**, *27*, 14–20. [CrossRef]
5. Schönherr, J.A.; Baumgartner, S.; Hartmann, M.; Stampfl, J. Stereolithographic additive manufacturing of high precision glass ceramic parts. *Materials* **2020**, *13*, 1492. [CrossRef] [PubMed]
6. Hou, J.; Xiao, Z.; Liu, Z.; Zhao, H.; Zhu, Y.; Guo, L.; Zhang, Z.; Ritchie, R.O.; Wei, Y.; Deng, X. An Amorphous Peri-Implant Ligament with Combined Osteointegration and Energy-Dissipation. *Adv. Mater.* **2021**, *33*, 2103727. [CrossRef]
7. Behera, R.P.; Ng, A.Y.R.; Reavley, M.J.H.; Du, Z.; Gan, C.L.; Le Ferrand, H. Rational design and fabrication of hierarchical ceramics using bioinspired microstructures for tailorable strength and toughness. *Cell Rep. Phys. Sci.* **2024**, *5*, 102140. [CrossRef]
8. Bregoli, C.; Biffi, C.A.; Tuissi, A.; Buccino, F. Effect of trabecular architectures on the mechanical response in osteoporotic and healthy human bone. *Med. Biol. Eng. Comput.* **2024**, *62*, 3263–3281. [CrossRef] [PubMed]
9. Mukasheva, F.; Adilova, L.; Dyussenbinov, A.; Yernaimanova, B.; Abilev, M.; Akilbekova, D. Optimizing scaffold pore size for tissue engineering: Insights across various tissue types. *Front. Bioeng. Biotechnol.* **2024**, *12*, 1444986. [CrossRef]
10. Lithoz GmbH. LithaLox 350—Alumina Slurry for Industrial & Medical Ceramics. 2025. Available online: https://www.lithoz.com/en/materials/lithalox-350/ (accessed on 9 October 2025).
11. Major, R.; Surmiak, M.; Kasperkiewicz, K.; Kaindl, R.; Byrski, A.; Major, Ł.; Russmueller, G.; Moser, D.; Kopernik, M.; Lackner, J.M. Antimicrobial materials with improved efficacy dedicated to large craniofacial bone defects after tumor resection. *Colloids Surf. B Biointerfaces* **2022**, *220*, 112943. [CrossRef]
12. Schwentenwein, M.; Homa, J. Additive manufacturing of dense alumina ceramics. *Int. J. Appl. Ceram. Technol.* **2015**, *12*, 1–7. [CrossRef]
13. Bai, R.; Sun, Q.; He, Y.; Peng, L.; Zhang, Y.; Zhang, L.; Lu, W.; Deng, J.; Zhuang, Z.; Yu, T.; et al. Ceramic Toughening Strategies for Biomedical Applications. *Front. Bioeng. Biotechnol.* **2022**, *10*, 840372. [CrossRef]
14. Li, H.; Liu, Y.; Liu, Y.; Hu, K.; Lu, Z.; Liang, J. Investigating the relation between debinding atmosphere and mechanical properties of stereolithography-based three-dimensional printed Al2O3 ceramic. *Proc. Inst. Mech. Eng. Part B J. Eng. Manuf.* **2020**, *234*, 1686–1694. [CrossRef]
15. Kermani, M.; Wu, J.; Liu, Z.; Zuo, F.; Lin, H.; Hu, C.; Grasso, S. Impact of sintering thermal history on MgO-doped alumina: Reduction of grain growth constant through high heating rates. *J. Am. Ceram. Soc.* **2024**, *107*, 132–143. [CrossRef]
16. Ali, A.; Chiang, Y.W.; Santos, R.M. X-Ray Diffraction Techniques for Mineral Characterization: A Review for Engineers of the Fundamentals, Applications, and Research Directions. *Minerals* **2022**, *12*, 205. [CrossRef]
17. Wu, H.L.; Li, H.; Cao, D.; Qiu, Y.; Wan, D.; Bao, Y. The Effects of Compressive Residual Stress on Properties of Kyanite-Coated Zirconia Toughened Alumina Ceramics. *Materials* **2023**, *16*, 6071. [CrossRef]
18. de Cerqueira Abud, I.; Barbosa, C.; de Jesus Monteiro, M.; Santos, C.T.D.; Gallo, G.O.; Caminha, I.M.V. Microstructural and Fractographic Aspects on the Failure Analysis of a Mixed Mode Fractured Ti-6Al-4V Femoral Long Plate. *J. Fail. Anal. Prev.* **2023**, *23*, 414–419. [CrossRef]
19. Srinivasan, T.; Suresh, G.; Ramu, P.; Vignesh, R.; Vijay Harshan, A.; Vignesh, K.P. Effect of hygrothermal ageing on the compressive behavior of glass fiber reinforced IPN composite pipes. *Mater. Today Proc.* **2021**, *45*, 1354–1359. [CrossRef]
20. Stephen Bernard, S.; Vivek, S.; Suresh, G.; Kannan, G.K. Influence of 3-(8,11,14-Pentadecatrienyl) Phenol Cardanol as a Bio-Based Binder in a Brake Pad. In *Advances in Design and Thermal Systems: Select Proceedings of ETDMMT 2020*; Springer: Singapore, 2021; pp. 519–527. [CrossRef]
21. Faisal, A.M.; Karthigeyan, L.; Suresh, G. Development of Conceptual Model for the Introduction Stage of Lean Intelligent Manufacturing Using Simulation Model Based on the Identification of the Appropriate Technologies of Industry 5.0. In *International Conference on Intelligent Manufacturing and Energy Sustainability*; Springer Nature: Singapore, 2024; pp. 237–246. [CrossRef]
22. Madheswaran, D.K.; Ganesamoorthy, R.; Selvi, S.; Vezhavendhan, R.; Ravi, R.; Suresh, G.; Chandramohan, P. An assessment of additive manufacturing technology for automotive and aerospace applications. *AIP Conf. Proc.* **2024**, *3122*, 100012. [CrossRef]
23. Kotteesvaran, B.; Vijayakumar, S.; Suresh, G.; Vimalanathan, P. A review on: Technologists interest on natural fibers. *AIP Conf. Proc.* **2024**, *3122*, 100026. [CrossRef]
24. Alharthi, F.; Wahab, R.; Manoharadas, S.; Alrayes, B.F.; Ahmad, N. Effect of preparation method and Ni^{2+} substitution on the structural, thermal, and optical properties of nanocrystalline lanthanum zirconate pyrochlore. *Crystals* **2021**, *11*, 1463. [CrossRef]
25. Fouda, A.M.; Bourauel, C.; Samran, A.; Kassem, A.S.; Alhotan, A. Effect of glazing and thermocycling on the fracture toughness and hardness of a New fully crystallized aluminosilicate CAD/CAM ceramic material. *BMC Oral Health* **2024**, *24*, 620. [CrossRef]
26. El-Tamimi, K.M.; Bayoumi, D.A.; Ahmed, M.M.Z.; Albaijan, I.; El-Sayed, M.E. The Effect of Salinized Nano ZrO2 Particles on the Microstructure, Hardness, and Wear Behavior of Acrylic Denture Tooth Nanocomposite. *Polymers* **2022**, *14*, 302. [CrossRef]
27. Serbanoiu, D.C.; Vartolomei, A.C.; Ghiga, D.V.; Pop, S.I.; Panainte, I.; Moldovan, M.; Sarosi, C.; Petean, I.; Boileau, M.J.; Pacurar, M. Comparative evaluation of dental enamel microhardness following various methods of interproximal reduction: A Vickers hardness tester investigation. *Biomedicines* **2024**, *12*, 1132. [CrossRef] [PubMed]

28. *ASTM C1424-15(2019)*; Standard Test Method for Monotonic Compressive Strength of Advanced Ceramics at Ambient Temperature. ASTM International: West Conshohocken, PA, USA, 2019. Available online: https://www.en-standard.eu (accessed on 17 November 2024).
29. Neher, S.H.; Klein, H.; Kuhs, W.F. Determination of crystal size distributions in alumina ceramics by a novel X-ray diffraction procedure. *J. Am. Ceram. Soc.* **2018**, *101*, 1381–1392. [CrossRef]
30. Chauruka, S.R.; Hassanpour, A.; Brydson, R.; Roberts, K.J.; Ghadiri, M.; Stitt, H. Effect of mill type on the size reduction and phase transformation of gamma alumina. *Chem. Eng. Sci.* **2015**, *134*, 774–783. [CrossRef]
31. Nasir, J.; Schmidt, F.; Menzel, F.; Schmedt auf der Günne, J. Structure and phase changes of alumina produced by flame hydrolysis. *Dalt. Trans.* **2024**, *53*, 14246–14257. [CrossRef]
32. Amrute, A.P.; Jeske, K.; Łodziana, Z.; Prieto, G.; Schüth, F. Hydrothermal Stability of High-Surface-Area α-Al2O3and Its Use as a Support for Hydrothermally Stable Fischer-Tropsch Synthesis Catalysts. *Chem. Mater.* **2020**, *32*, 4369–4374. [CrossRef]
33. Burger, W.; Kiefer, G. Alumina, Zirconia and Their Composite Ceramics with Properties Tailored for Medical Applications. *J. Compos. Sci.* **2021**, *5*, 306. [CrossRef]
34. Zhang, Y.; Lawn, B.R. Novel Zirconia Materials in Dentistry. *J. Dent. Res.* **2018**, *97*, 140–147. [CrossRef]
35. Huang, B.; Chen, M.; Wang, J.; Zhang, X. Advances in zirconia-based dental materials: Properties, classification, applications, and future prospects. *J. Dent.* **2024**, *147*, 105111. [CrossRef] [PubMed]
36. Khanlar, L.N.; Rios, A.S.; Tahmaseb, A.; Zandinejad, A. Additive manufacturing of zirconia ceramic and its application in 19 clinical dentistry: A review. *Dent. J.* **2021**, *9*, 104. [CrossRef] [PubMed]
37. Bishwas, R.K.; Alam, M.A.; Jahan, S.A. Crystallographic and morphological characterization of high-crystalline α-alumina 27 nanoparticles: A comprehensive X-ray diffraction and transmission electron microscopy study. *Chem. Phys. Lett.* **2025**, *878*, 142245. [CrossRef]
38. Peintinger, M.F.; Kratz, M.J.; Bredow, T. Quantum-chemical study of stable, meta-stable and high-pressure alumina pol-30 ymorphs and aluminum hydroxides. *J. Mater. Chem. A* **2014**, *2*, 13143–13158. [CrossRef]
39. Ciobanu, C.S.; Predoi, D.; Iconaru, S.L.; Negrila, C.C.; Leduc, D.; Ghegoiu, L.; Bleotu, C.; El Kettani, M.E.C.; Trusca, R.; Zelmar, P.; et al. New Nanobioceramics Based on Hydroxyapatite for Biomedical Applications: Stability and Properties. *Nanomaterials* **2025**, *15*, 224. [CrossRef]
40. Arena, A.; Prete, F.; Rambaldi, E.; Bignozzi, M.C.; Monaco, C.; Di Fiore, A.; Chevalier, J. Nanostructured zirconia-based ceramics and composites in dentistry: A state-of-the-art review. *Nanomaterials* **2019**, *9*, 1393. [CrossRef]
41. Polat Sağsöz, N.; Murat, F.; Sevinç Gül, S.N.; Şensoy, A.T.; Kaymaz, I. CF-PEEK vs. Titanium Dental Implants: Stress Distribution and Fatigue Performance in Variable Bone Qualities. *Biomimetics* **2025**, *10*, 619. [CrossRef]
42. Sanjuán, M.; Brizuela-Velasco, A.; Gil, J.; Cerrolaza, M.; Montalvillo, E.; Fernández-Hernández, S.; Robles, D. Hybrid surface implants: Influence of residual stress on mechanical behavior, evaluated by finite element analysis and validation by fatigue tests. *Dent. Mater.* **2024**, *40*, 9–18. [CrossRef]
43. Deb, A.K.; Chatterjee, P. Estimation of lattice strain in alumina–zirconia nanocomposites by X-ray diffraction peak profile analysis. *J. Theor. Appl. Phys.* **2019**, *13*, 221–229. [CrossRef]
44. Thanigachalam, M.; Subramanian, A.V.M. Fabrication, microstructure and properties of advanced ceramic-reinforced 32 composites for dental implants: A review. *Biomater. Transl.* **2023**, *4*, 151–165. [CrossRef]
45. Hofer, A.K.; Kraleva, I.; Bermejo, R. Additive manufacturing of highly textured alumina ceramics. *Open Ceram.* **2021**, *5*, 100085. [CrossRef]
46. Munenge, E.; Mtetwa, W.; Ngwangwa, H.M.; Pandelani, T.; Lebea, L. Compression behavior of alumina (Al_{23}) ceramic for bio-inspired 3D-printed dental implants. In *Engineering Materials, Structures, Systems and Methods for a More Sustainable Future*; CRC Press: Boca Raton, FL, USA, 2025; pp. 1095–1099. [CrossRef]
47. Lang, Y.; Zhao, L.; Dai, X.; Wang, C.A. Effect of alumina fiber content on pore structure and properties of porous ceramics. *Int. J. Appl. Ceram. Technol.* **2019**, *16*, 814–819. [CrossRef]
48. Zhao, Y.; Deng, J.; Li, W.; Liu, J.; Yuan, W. Grain growth behavior of alumina in zirconia-toughened alumina (ZTA) ceramics 37 during pressureless sintering. *Crystals* **2025**, *15*, 89. [CrossRef]
49. Sotova, C.; Yanushevich, O.; Kriheli, N.; Grigoriev, S.; Evdokimov, V.; Kramar, O.; Nozdrina, M.; Peretyagin, N.; Undritsova, N.; Popelyshkin, E.; et al. Dental Implants: Modern Materials and Methods of Their Surface Modification. *Materials* **2023**, *16*, 7383. [CrossRef]
50. Dejak, B.D.; Langot, C.; Krasowski, M.; Klich, M. Evaluation of hardness and wear of conventional and transparent zirconia ceramics, feldspathic ceramic, glaze, and enamel. *Materials* **2024**, *17*, 3518. [CrossRef]
51. Labetić, A.; Klaser, T.; Skoko, Ž.; Jakovac, M.; Žic, M. Surface hardness of polished dental zirconia: Influence of polishing and yttria content on morphology, phase composition, and microhardness. *Materials* **2025**, *18*, 3380. [CrossRef] [PubMed]
52. Patil, A.; Davidson Jebaseelan, D.; Bomze, D.; Gopal, V. Wear behaviour of lithography ceramic manufactured dental zir-46 conia. *BMC Oral Health* **2023**, *23*, 276. [CrossRef]

53. Upadhyay, A.; Pradhan, L.; Yenurkar, D.; Kumar, K.; Mukherjee, S. Advancement in ceramic biomaterials for dental im plants. *Int. J. Appl. Ceram. Technol.* **2024**, *21*, 2796–2817. [CrossRef]
54. Piconi, C.; Sprio, S. Oxide bioceramic composites in orthopedics and dentistry. *J. Compos. Sci.* **2021**, *5*, 206. [CrossRef]

Disclaimer/Publisher's Note: The statements, opinions and data contained in all publications are solely those of the individual author(s) and contributor(s) and not of MDPI and/or the editor(s). MDPI and/or the editor(s) disclaim responsibility for any injury to people or property resulting from any ideas, methods, instructions or products referred to in the content.